Structural, Microstructure, Dielectric relaxation and AC conduction studies of perovskite $SrSnO_3$ and Ruddlesden Popper oxide Sr_2SnO_4

Manisha Jatiya[1#], Vedika Yadav[1#], Upendra Kumar[1*], Abhishek Kumar Singh[2], Shalu[3]

Advanced Functional Materials Laboratory, Department of Applied Science, IIIT Allahabad, Prayagraj, Uttar Pradesh 211015, India

Electrical and Electronics Department, Rajiv Gandhi Institute of Petroleum Technology, Amethi 229305, India

Department of Physics, Sharda School of Basic Sciences & Research, Sharda University, Greater Noida-201306, Uttar Pradesh, INDIA

#: Equal Author Contribution; Corresponding Author*: upendra.bhu512@gmail.com

Supplementary File

S1. Study of phase formation and crystal structure

The phase formation of samples was studied by recording the XRD pattern of both samples obtained at as prepared, 1000°C, 1200°C and 1350°C and shown in Fig. S1. The as prepared XRD pattern of both samples shows the unreacted raw materials $SrCO_3$ and SnO_2. However, the pattern obtained at 1000°C indicate the formation of phase $SrSnO_3$ with tiny amount of $SrCO_3$ and SnO_2 (indicated by @ and #). Further increase of temperature to 1200°C results the single-phase formation of both phase $SrSnO_3$ and Sr_2SnO_4. Further increasing the temperature, the diffraction pattern of both the samples shows increase of the intensity as well as the sharpness of peaks. The reported crystallographic open database (COD) numbers 1530998 for $SrSnO_3$ and 1539931 for Sr_2SnO_4 are well matched with all of the diffraction peaks present in both samples [1,2].

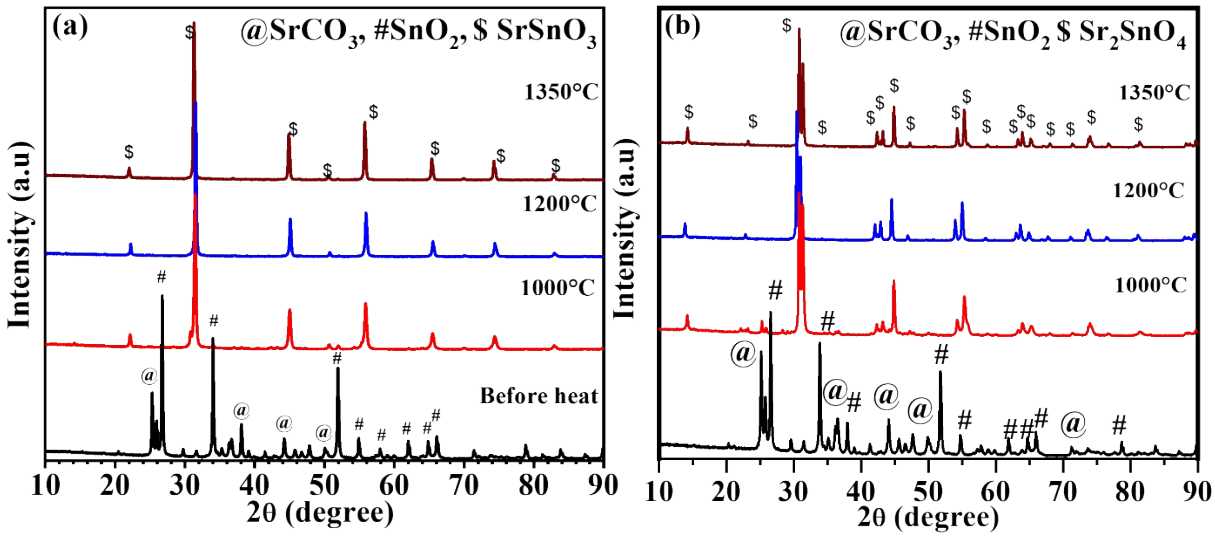

Fig. S1: Room temperature XRD pattern of samples at different temperatures **(a)** SSO, **(b)** S2SO.

S1.1 Evaluation of crystallite size and micro-strain.

The XRD peak's broadening suggests the presence of a number of factors, including instrumental broadening, microstrain, and lower crystallite sizes. By using the Debye-Scherrer formula, the crystallite size of the samples was linked with the fullwidth half maximum (FWHM) of the XRD peak [3]:

$$D = \frac{k\lambda}{\beta\ COS\ \theta_{max}} \quad (3)$$

Here λ denotes the wavelength (1.54Å for Cu-kα radiation) of X-ray, β is the FWHM of XRD peak in radian and k is Scherrer's constant equivalent to 0.94. Since the FWHM peak has several contributions, so it can't be used directly in eq. (3). In order to correct the FWHM of sample's XRD peak from instrumental broadening, it is necessary to obtained a XRD pattern of Si-single crystal. Now, the corrected β can be obtained by following eq [4]:

$$\beta^2 = \beta^2_{measured} - \beta^2_{instrumental} \quad (4)$$

The crystallite size for samples SSO1, SSO2, S2SO1, and S2SO2 was determined by eq. (5) using β from eq. (6) and given in Table S1. In comparison to the sample S2SO exhibit larger crystallite size than SSO. The obtained value of crystallite size may not be accurate, as the contribution of micro-strain was not separated from the FWHM of XRD peak. The literature suggests an alternative approach to determine crystallite size and micro-strain, name "Size-Strain Plot" (SSP) [5]. The SSP plot uses a Lorentzian function to represent the crystallite size of samples and a Gaussian function to represent strain. The SSP method was mathematically represented by following equation [6]:

$$\left(\frac{d_{hkl}\beta cos\theta}{\lambda}\right)^2 = \frac{k\lambda}{D}\left(\frac{d^2_{hkl}\beta cos\theta}{\lambda^2}\right) + \left(\frac{\varepsilon}{2}\right) \quad (5)$$

Here d_{hkl} denotes the interplanar spacing equivalent to the plane (hkl), variable ε represents the micro-strain induced in the lattice, and the parameter β, λ and D is same as define in the Debye-Scherrer's equation and k denotes the Scherrer constant which is equal to 3/4. The plot of $\left(\frac{d_{hkl}\beta cos\theta}{\lambda}\right)^2$ versus $\left(\frac{d^2_{hkl}\beta cos\theta}{\lambda^2}\right)$ for SSO and S2SO are shown in Fig. S2.

The slope and intercept of the fitted curve (shown by the red line) were used to calculate the crystallite size and micro-strain values, while the slope of the graphs and the square root of the

intercept were used to get the lattice strain values. Table S1 displays the lattice strain and crystallite size obtained from SSP plots for the two samples. Table S1 shows that, despite following a similar pattern, the value of crystallite size obtained via SSP was larger than Debye-Scherrer. Williamson-Hall (W-H) plot was another literary strategy that was covered.

Moreover, it is noted that the crystallite size and microstrain of S2SO were found to be higher than those of SSO. Another parameter named "**Dislocation density**" is also an important parameter in materials characterization which is defined as the number of dislocations in a unit volume of a crystalline material. The dislocation density can be calculated by formula [7]:

$$\delta = \frac{1}{D^2} \qquad (6)$$

Here, D is the dimension of the crystal (obtained from W-H plot). Table S1 displays the value of dislocation density obtained using eq. (6). Dislocation density was observed to be less for SSO2 than SSO1, and remains same for S2SO1 and S2SO2. It is a well-known phenomenon that, as crystallite size decreases, dislocation density increases, and vice versa. Thus, here we say that the phase $SrSnO_3$ has lower dislocation density than Sr_2SnO_4.

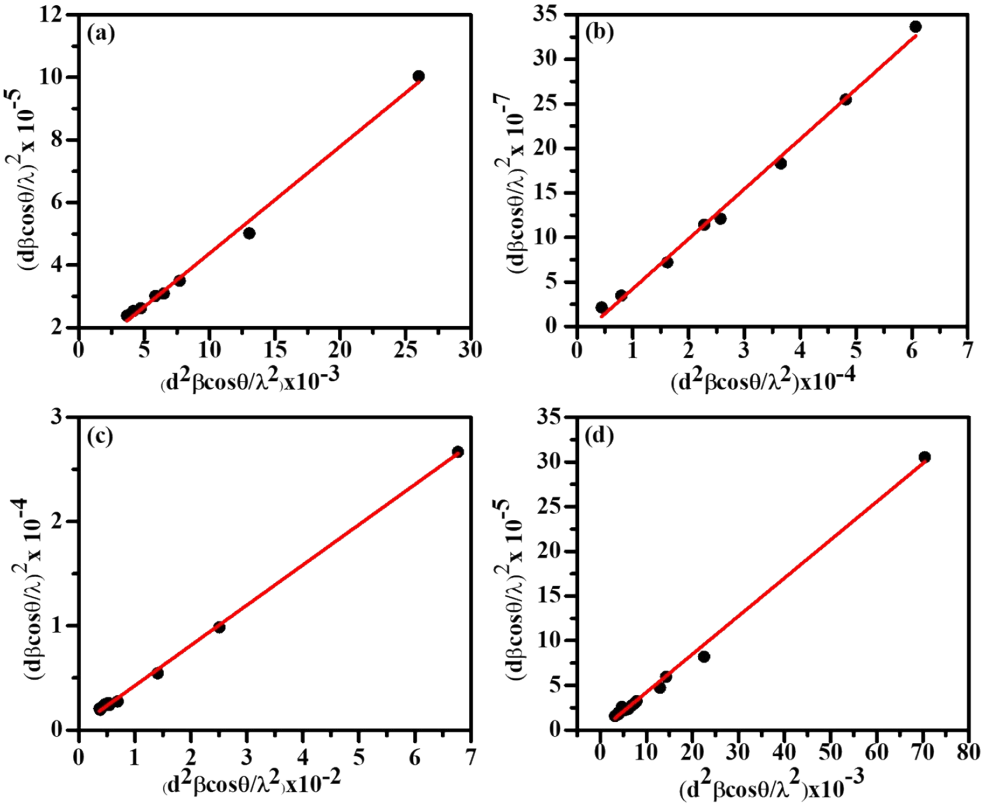

Fig. S2: Size-strain plot of samples, **(a)** SSO1, **(b)** SSO2, **(c)** S2SO1, **(d)** S2SO2 obtained using eq. (5).

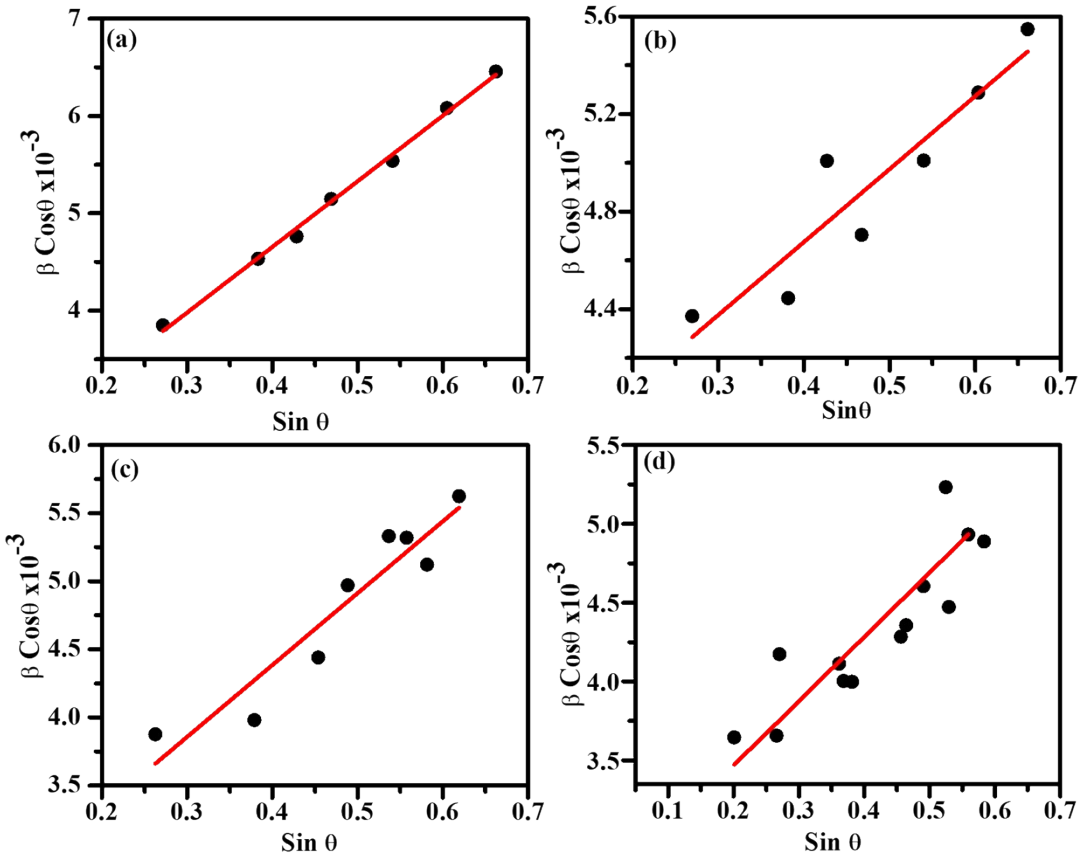

Fig. S3: Williamson–Hall plot of sample **(a)** SSO1, **(b)** SSO2, **(c)**S2SO1, **(d)** S2SO2 generated using eq. (6).

Table S1: Comprehensive analysis of crystallite size, microstrain, and dislocation density across all samples.

S. No.	Sample name	Crystallite size (nm)			Strain (ε)×10^{-3}		Dislocation Density (m^{-3}) (x 10^{14})
		Debye-Scherrer	W-H plot	SSP plot	W-H plot	SSP plot	
1.	SSO1	28.79	73.75	40.97	6.71	6.192	8.75
2.	SSO2	28.73	42.72	25.02	3.35	0.369	4.64
3.	S2SO1	33.79	61.73	40.97	5.28	4.090	12.05
4.	S2SO2	46.38	52.50	32.81	4.02	0.566	12.11

S2. Variation of power exponent as function of temperature

The conduction and relaxation process has been further explored from the thermal variation of power exponent (n) as described in literature [8]. The fluctuation of n as a function of temperature is seen in Fig. S4. The strength between the host lattice and the mobile charge carrier, as well as the dimension of conduction, are both represented by the power exponent. In order to

investigate the conduction and relaxation mechanisms involved in the sample, several models were explored in the literature. Here is a list of those models;

1. Applications of the quantum mechanical tunnelling (QMT) model were made to systems where the power exponent n is frequency-dependent but temperature-independent.
2. For systems where the power exponent n rises with temperature, the non-overlapping small-polaron tunnelling (NSPT) model was used.
3. When exponent n initially falls with temperature, reaches a minimal value, and subsequently grows with temperature, the overlapping of large polaron tunnelling (OLPT) model was used.
4. When the barrier height is independent of intersite separation, the hopping over barrier (HOB) model was used, and the value of the frequency exponent n is projected to be unity.
5. When the value of the exponent n decreases with increasing temperature, the correlated barrier hopping (CBH) model was used.

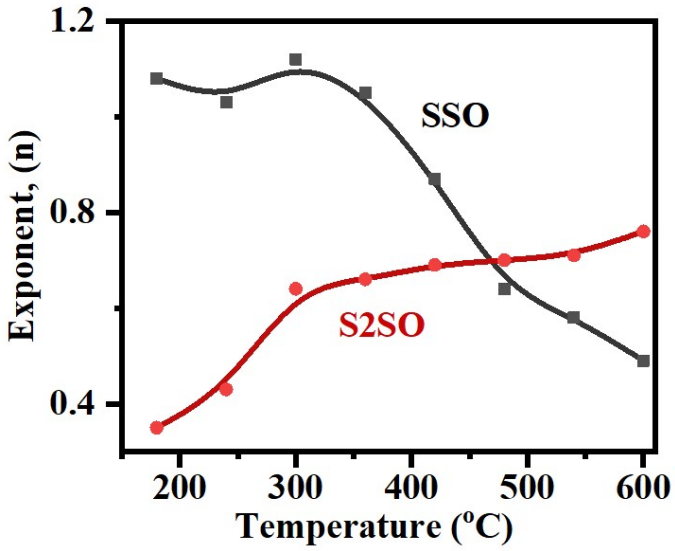

Fig. S4: Variation of power exponent, n with temperature.

Based on the variation observed in power exponent with temperature for sample SSO indicate decrease in n with increasing temperature suggesting correlated barrier hopping (CBH) [9]model suitable explain the conduction and relaxation mechanism involved in it, whereas for S2SO, the value of power exponent n increases with temperature suggesting nearly small polaron tunneling (NSPT) model [10]suitably explain the conduction and relaxation process involved in it. Since both has different crystal structure as well as their size and dislocation density, which might be the possible reason for difference in conduction mechanism.

In CBH model the conduction between two sites such as $V_O^{\cdot\cdot} - Sn_{Sn^{4+}}^{2+\,\prime}$ takes place via crossing the barrier potential (formed by $V_O^{\cdot\cdot}$ and $Sn_{Sn^{4+}}^{2+\,\prime}$) through hopping of electron between Sn-sites or via orientation of dipole to the vacant sites (see activation energy given in inset of Figure). However, in NSPT model the conduction and relaxation process takes place via the overlapping of the wavefunction associated with the potential barrier site with increasing temperature via the transfer of electron between Sn-sites (see activation energy given in inset of Figure).

S3. Modulus Spectroscopy studies

Fig. S5 depicts the real part of the electric modulus (M') in the frequency range (1 Hz – 2 MHz) from temperature 180 °C to 600 °C for both samples. The modulus spectrum shows three distinct regions suggesting the various kinds of behaviour of charge carrier in the frequency range. Region first observed below 100 Hz, second in between 101 Hz to 10 KHz and the third one observed above 10 KHz. The region 1 observed at different temperature approaches zero exclude the contribution of the electrode sample contribution from the interfacial polarization (as discussed in dielectric properties section) [11]. Region-2, a dispersion region founds to be shifted towards higher frequency with increasing temperature suggests a thermally dependent relaxation process in the sample while region 3 indicates a higher value of M' suggesting the diminutive nature of forces governed by the mobility of charge carrier under the presence of field.

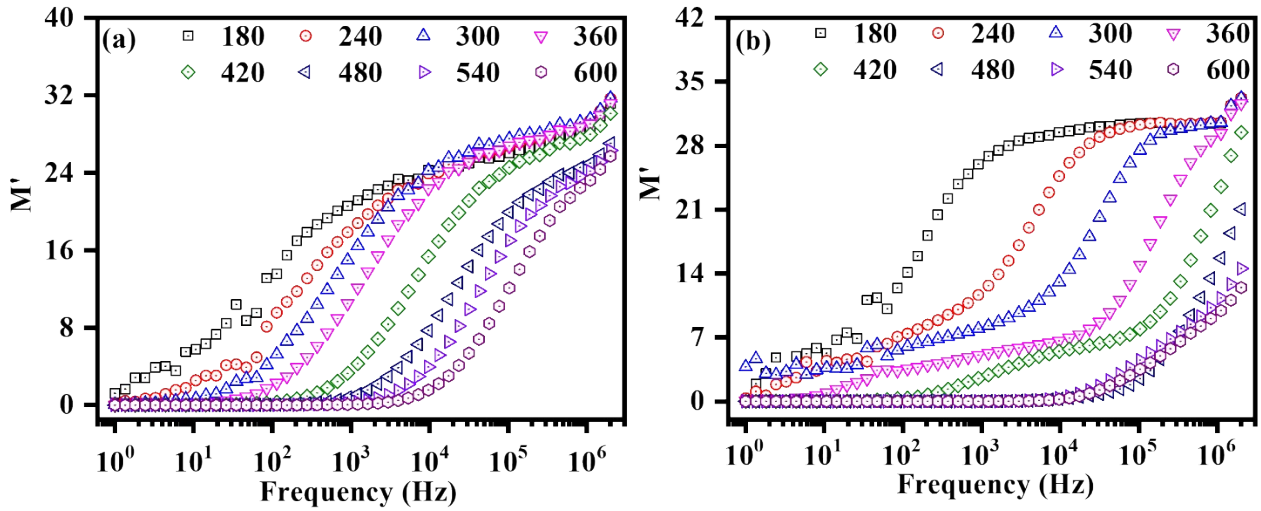

Fig. S5: Variation in real part of modulus (M') as a function frequency at different temperatures **(a)** SSO, **(b)** S2SO.

Further to study the conduction and relaxation process whether having similar mechanism or not, the imaginary part of impedance (Z'') and modulus (M'') were shown as a function of frequency at different temperatures for sample SSO in Fig. S6 and for sample S2SO in Fig. S7. It has been observed from both figure that with increasing temperature the separation between the Z'' and M'' exist at all temperature with reducing the gap between it for both sample which suggests that the relaxation mechanism and conduction mechanism even though having similar kinds of charge carrier but they had different localized motion (mobility of charge carrier) [12].

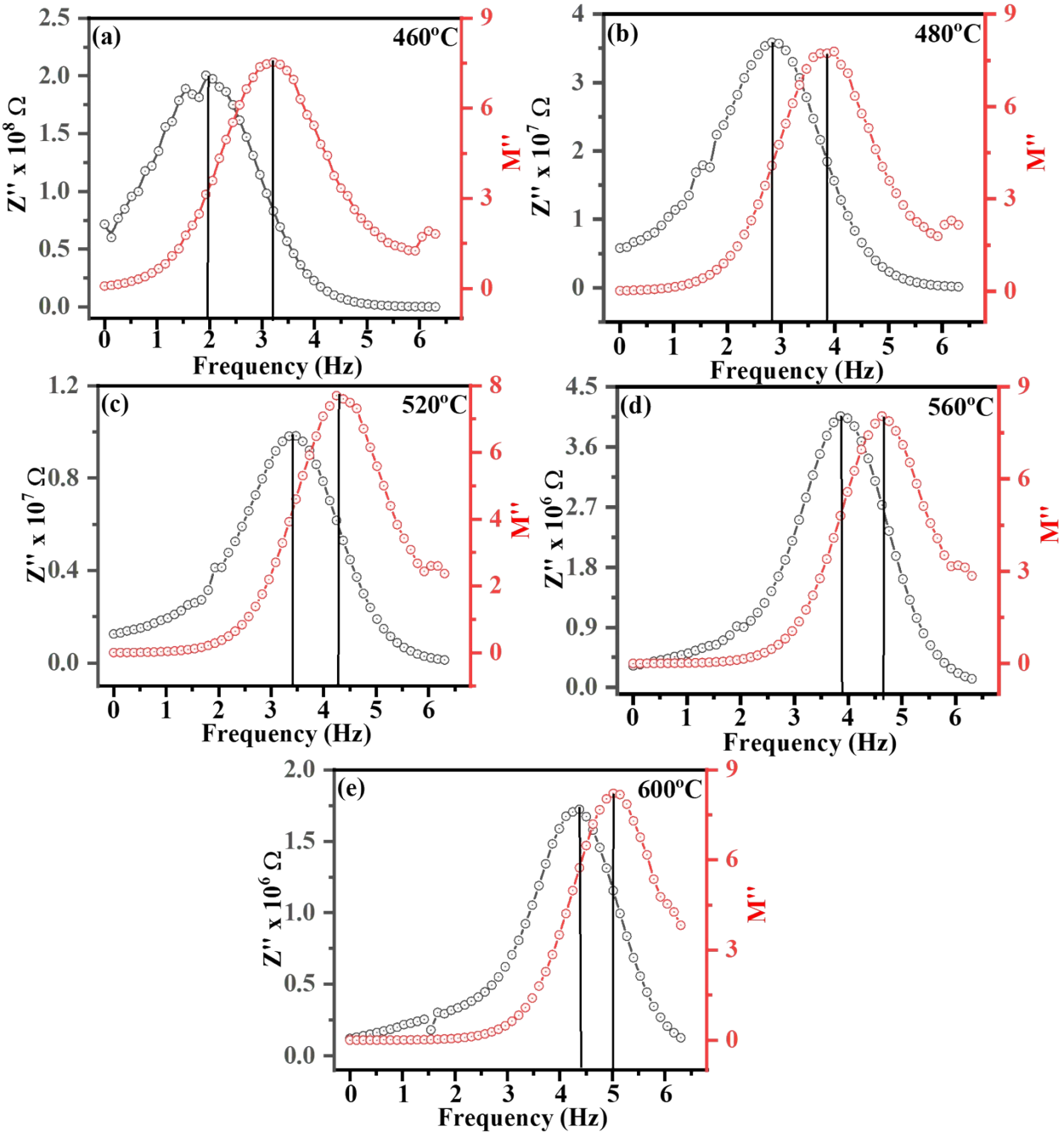

Fig. S6: Variation of Z''/M'' with $\log f$ at different temperature for sample SSO.

On comparing with both structures, it has been noticed that the gap between Z'' and M'' in SSO is larger whereas in S2SO it is small which might be due to either larger hopping of charge carrier or lighter charge carrier concentration (electronic migration). This reconfirms the assumption made in the conductivity study.

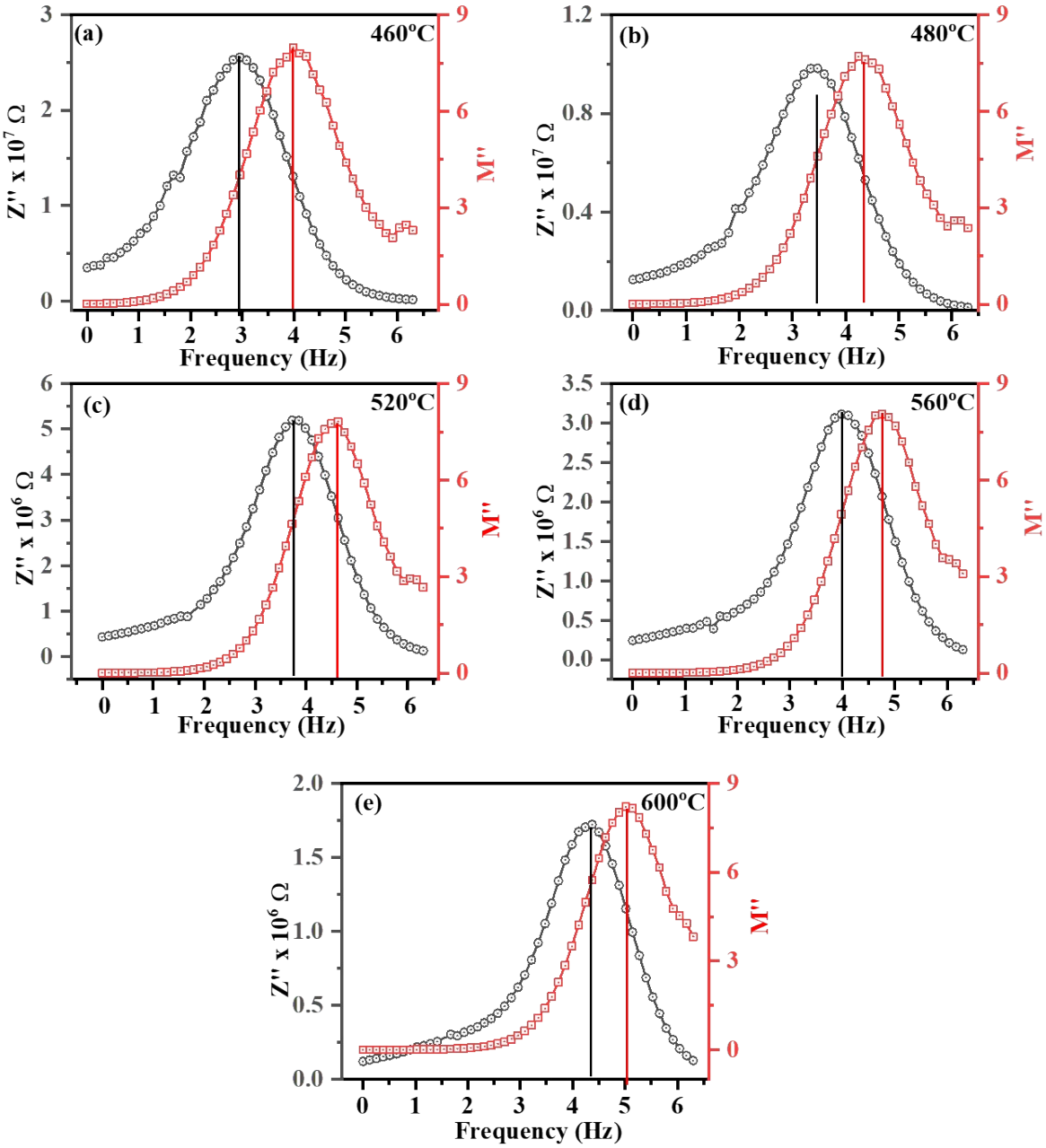

Fig. S7: Variation of Z''/M'' with $\log f$ at different temperature for sample S2SO.

Thus here, we say that even though the charge carriers remain same in conduction and relaxation process but they had differed in charge carrier concentration or the mobility of the charge carrier.

References

1 S. Li-Wei, D. Yi-Feng, Y. Xian-Qing and Q. Li-Xia, Structural, electronic and elastic properties of cubic perovskites srsno3 and srzro3 under hydrostatic pressure effect, *Chinese Phys. Lett.*, 2010, **27**, 96201.

2 U. Kumar and S. Upadhyay, Studies on dielectric and electrical properties of Ruddlesden-Popper oxide Sr2SnO4, *Mater. Lett.*, 2018, **227**, 100–103.

3 S. Sarkar and R. Das, Determination of structural elements of synthesized silver nano-hexagon from X-ray diffraction analysis, *Indian J. Pure Appl. Phys.*, 2018, **56**, 765–772.

4 Y. Zhao and J. Zhang, Microstrain and grain-size analysis from diffraction peak width and graphical derivation of high-pressure thermomechanics, *J. Appl. Crystallogr.*, 2008, **41**, 1095–1108.

5 A. K. Zak, W. H. A. Majid, M. E. Abrishami and R. Yousefi, X-ray analysis of ZnO nanoparticles by Williamson–Hall and size–strain plot methods, *Solid State Sci.*, 2011, **13**, 251–256.

6 T. Maiti, R. Guo and A. S. Bhalla, Evaluation of experimental resume of BaZrxTi1-xO 3 with perspective to ferroelectric relaxor family: An overview, *Ferroelectrics*, 2011, **425**, 4–26.

7 M. A. Shukur, K. V. Kumar and G. N. Rao, Impact of annealing temperature on Optical parameters of La0. 25Sr0. 75MnO3 nano Crystallites.

8 D. N. Singh, T. P. Sinha and D. K. Mahato, Electric modulus, scaling and ac conductivity of La2CuMnO6 double perovskite, *J. Alloys Compd.*, 2017, **729**, 1226–1233.

9 K. Prasad, Lily, K. Kumari, K. P. Chandra, K. L. Yadav and S. Sen, Electrical properties of a lead-free perovskite ceramic:(Na 0.5 Sb 0.5) TiO 3, *Appl. Phys. A*, 2007, **88**, 377–383.

10 D. Singh and A. Mahajan, Synthesis and characterization of Ruddlesden–Popper oxides Nd1+ xSr2− xMnCrO7 (x= 0.0, 0.2 and 0.4), *Ceram. Int.*, 2015, **41**, 15048–15056.

11 U. Kumar, K. Ankur, D. Yadav and S. Upadhyay, Synthesis and characterization of Ruddlesden-Popper system (Ba1−xSrx)2SnO4, *Mater. Charact.*, 2020, **162**, 110198.

12 Y. Singh and S. Singh, Electric field-temperature phase diagram and electrical properties of (1-x) Na0. 5Bi0. 5TiO3-xK0. 5Bi0. 5TiO3 ceramics, *Mater. Sci. Eng. B*, 2023, **297**, 116788.